

# Dynamics, Design and Simulation of a Novel Microrobotic Platform Employing Vibration Microactuators

Panagiotis Vartholomeos  
Evangelos Papadopoulos

Department of Mechanical Engineering,  
National Technical University of Athens,  
Athens 157 80, Greece

*This paper presents the analysis, design, and simulation of a novel microrobotic platform that is able to perform translational and rotational sliding with submicrometer positioning accuracy and develop velocities up to 1.5 mm/s. The platform actuation system is novel and based on centripetal forces generated by vibration micromotors. The motion principle is discussed in detail, and the dynamic model of the platform and of its actuation system is developed. Analytical expressions for the distinct modes of operation of the platform are derived and used to provide system design guidelines. Simulations are performed that verify the analytical results, demonstrate the platform capabilities, and examine its transient response. The microrobot design is simple, compact, and of low cost. In addition, the energy supply of the mechanism can be accomplished in an untethered mode using simple means, such as single-cell batteries. [DOI: 10.1115/1.2168472]*

*Keywords:* miniature robot, micropositioning, vibration motors

## 1 Introduction

In the last decade, microrobotics has become an increasingly important field of research. Domains of application, such as microfabrication, biotechnology, microscopy and optoelectronics, demand miniaturized or microrobotic platforms that provide ultra-high precision, flexibility, and a wide mobility range. Furthermore, scientists that are involved to the emerging nanotechnology will require variety of novel tools to probe and manipulate their invisible specimens. To this aim, extensive research has been carried out in the design and realization of micromanipulators and microrobots (a robot so named not because it has microdimensions itself but because it can manipulate specimens with nanometer and micrometer accuracy). Motion principles and actuation mechanisms that combine submicrometer motion of high resolution and the speed virtues of coarse positioning have been the subject of intensive studies.

Several microactuation techniques have been devised and are usually based on smart materials such as piezoelectric actuators, shape memory alloys, etc. The most popular micropositioning motion mechanism is the stick-slip principle [1], which is implemented using piezoelectric actuators. This principle is employed by the 3-DOF (degree-of-freedom) microrobotic platform presented in [1] and by the MINIMAN microrobot presented in [2,3]. These platforms are capable of positioning accuracy of <200 nm and provide velocities of up to a few millimeters per second. The impact-drive principle (a variant of the stick-slip principle) is employed by the 3-DOF microrobotic platform Avalon, which provides a step size of about  $3.0 \mu\text{m}$  and speeds up to 1 mm/s and is presented in [4,5]. A different motion mechanism based on piezotubes is utilized by the Nano Walker microrobot presented in [6]. The first prototypes of this microrobot were capable for minimum steps of the order of 30 nm and demonstrated a maximum displacement rate of 200 mm/s. Also, interesting is the extensive work on the development of miniature multilayer actuators and

the analysis of the walking principle presented in [7–9]. A motion principle based on piezoactuators and electromagnets is presented in [10], where the interaction of piezoelectric elements and electromagnetic actuators results in a step length of  $7.0 \mu\text{m}$  and a velocity of 1.16 mm/s. Furthermore, [11] describes an earthwormlike locomotion principle implemented using shape memory alloys.

Although piezoelectric actuators seem to be the favored smart material for micropositioning and do provide the required positioning resolution and actuation response, they usually suffer from complex power units that are expensive and cumbersome and that do not easily allow for untethered operation. Furthermore, piezoelectric actuators are complex systems that exhibit nonlinear behavior and, as a result, they lack accurate mathematical model that can provide a reliable prediction of the system's behavior. A novel and low-cost alternative approach is the six-axis nanomanipulator presented in [12], which is based on a single-piece, flexible construction. An interesting unconventional motion principle that employs inverse pendulum dynamics is presented in [13]. Miniature robotic platforms of relatively low cost have been built by [14]. These platforms employ wheels, which limit the repeatability and the resolution of motion.

The thrust of this paper is in analyzing and presenting the expected dynamic behavior of vibration microrobots and can be used for developing such devices. The theoretical model of the robotic platform suggests that it is able to perform translational and rotational sliding with submicrometer positioning accuracy and velocities up to 1.5 mm/s. All the components of the mechanism, including its driving units, are of low cost and readily available. The motion mechanism is based on the interaction of centripetal forces generated by platform-mounted vibration micromotors and friction forces at the supports of the same platform. The concept was inspired by observing the motion of devices that vibrate, such as cellular phones or unbalanced washing machines [15,16]. The microrobotic platform presented in this paper is novel primarily due to its motion mechanism, which, to the extent of the authors knowledge, has not been studied until now.

Contributed by the Dynamic Systems, Measurement, and Control Division of ASME for publication in the JOURNAL OF DYNAMIC SYSTEMS, MEASUREMENT, AND CONTROL. Manuscript received April 1, 2005; final manuscript received November 15, 2005. Assoc. Editor: Sunil K. Agrawal.

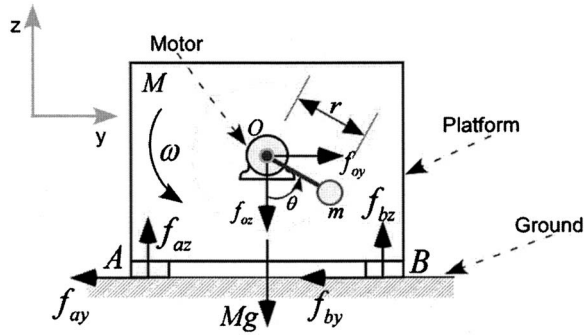


Fig. 1 Simplified 1-DOF platform with rotating mass  $m$

Innovative is also the design of the platform, which allows for multidirectional, ultraprecise sliding motion with low-cost driving units.

First, analysis of the motion principle physics is provided. Then, rigid and deformable body dynamic models of the platform are developed. The dynamics of the DC vibration micromotors are considered also. Analytical expressions for the distinct modes of operation of the platform are derived and used to provide system design guidelines. A commercial vibration micromotor is selected that complies with the derived guidelines. Using a basic platform design, simulations are performed that verify the analytical results, demonstrate the platform modes of operation, and examine the transient effects that the platform may exhibit. Finally, a set of equations for open-loop control of the platform are derived and tested through the execution of a simple sequence of trajectories.

## 2 Motion Principle

The motion principle is first demonstrated using a simplified single-degree-of-freedom mobile platform of mass  $M$ . The motion mechanism employs an eccentric mass  $m$  rotated by a motor  $O$  mounted on the platform as shown in Fig. 1.

It is assumed that the mass  $m$  rotates on a vertical plane at constant angular speed  $\omega$ , about point  $O$ , and that the platform is constrained to move only along the  $y$ -axis. One cycle of operation is completed when the mass has described an angle of 360 deg. Gravitational and centripetal forces exerted on the rotating mass are resolved along the  $y$ - $z$  axis to yield

$$\begin{aligned} f_{oy} &= mr\omega^2 \sin \theta \\ f_{oz} &= -mg = mr\omega^2 \cos \theta \end{aligned} \quad (1)$$

where  $g$  is the acceleration of gravity and  $r$  the length of the link between  $m$  and  $O$ . These forces are also applied to the platform at point  $O$ , while the moment due to the small eccentric mass is neglected. When the angular speed  $\omega$  is low, the platform does not move because the horizontal actuation force  $f_{oy}$  is cancelled by frictional forces at the platform contact points  $A$  and  $B$ . However, if the angular speed  $\omega$  exceeds a critical value, then  $f_{oy}$  overcomes the Coulomb friction forces applied at the two support points, and as a result, the platform begins to slide.

Using a simplified static-kinetic friction model [17], the motion of the platform along the  $y$  and  $z$  axes is described by the following equations:

$$\begin{aligned} M\ddot{y} &= f_{oy} - f_{fr} \\ 0 &= f_{az} + f_{bz} + (-Mg + f_{oz}) \end{aligned} \quad (2)$$

where all forces are defined in Fig. 1,  $M$  is the mass of the platform, and  $f_{fr}$  is the friction force. Neglecting viscous friction, the friction force is given by

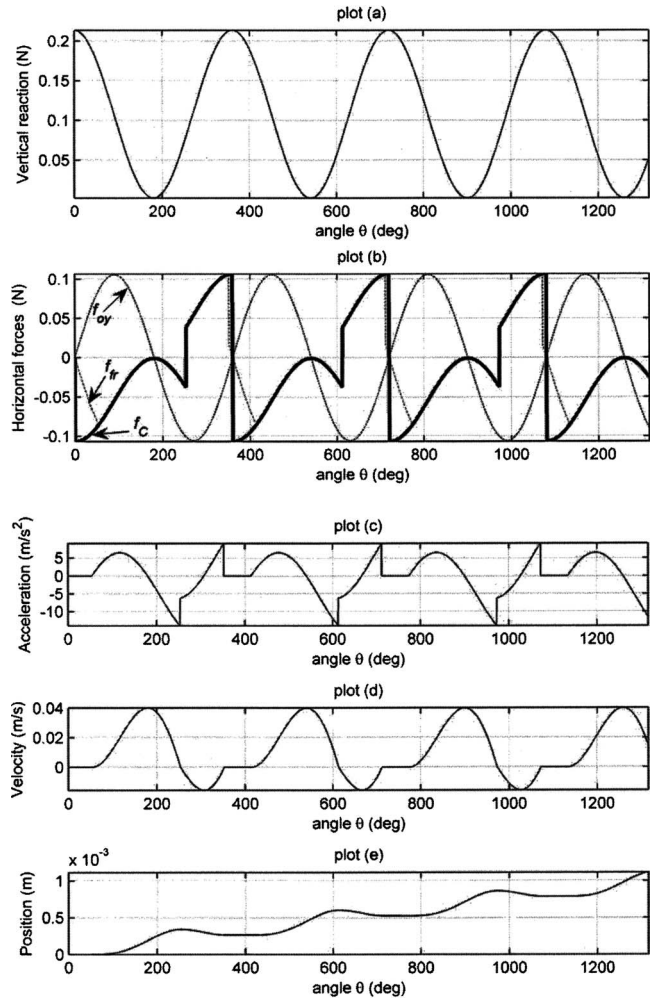


Fig. 2 Forces applied to the 1-DOF platform

$$f_{fr} = \begin{cases} f_C \operatorname{sgn}(\dot{y}), & \dot{y} \neq 0 \\ f_{oy}, & \|f_{oy}\| < f_C, \dot{y} = 0, \ddot{y} = 0 \\ f_C \operatorname{sgn}(f_{oy}), & \|f_{oy}\| > f_C, \dot{y} = 0, \ddot{y} \neq 0 \end{cases} \quad (3)$$

where  $f_C$  is the Coulomb friction level, i.e., the maximum friction force that can exist for the current normal force, and is given by

$$f_C = \mu(f_{az} + f_{bz}) = \mu(Mg - f_{oz}) \quad (4)$$

and the viscous friction is neglected. The parameter  $\mu$  is the coefficient of kinetic friction and the function  $\operatorname{sgn}(\dot{y})$  is defined by

$$\operatorname{sgn}(\dot{y}) = \begin{cases} +1, & \dot{y} > 0 \\ 0, & \dot{y} = 0 \\ -1, & \dot{y} < 0 \end{cases} \quad (5)$$

To gain some insight into the behavior of the platform-rotating-eccentricity system, its response is obtained by means of a numerical simulation and the results are displayed in Fig. 2. Figure 2(a) depicts the time response of the sum of the vertical forces exerted on the platform, i.e., the actuation force component  $f_{oz}$  plus the gravitational force  $Mg$ . This sum is equal in magnitude to the support reaction forces and is time periodic because it includes a sinusoidal and a DC component. Because of Eq. (4), the same applies to the Coulomb friction level  $f_C$ . In Fig. 2(b) the magnitude of the black thick curve is given by  $f_C$ , but its sign changes from positive to negative, depending on the speed direction. This

figure also shows the horizontal forces that act on the platform, namely, the horizontal actuation force  $f_{oy}$  and the friction force  $f_{fr}$ .

Figure 2(c) depicts the acceleration of the platform  $\ddot{y}$ , computed using Eqs. (2)–(5), while Fig. 2(d) depicts its velocity, and Fig. 2(e) its displacement. From Figs. 2(b) and 2(d), it is clear that motion is induced when the horizontal actuation force overcomes the static friction limit  $f_C$ . Quite interestingly, as shown in Fig. 2(e) for a counterclockwise rotation of the motor, the platform exhibits a net displacement along the positive  $y$ -axis.

The physics of the motion principle are explained next, in more detail. When the eccentric mass is at the lower points of its trajectory, the normal forces (and therefore, the frictional forces) are high, whereas when the eccentric mass is at its highest points, the frictional forces are low. Accordingly, for counterclockwise rotation of mass  $m$  initiated at  $\theta=0$  deg, the platform tends not to move when  $m$  is low and to move to the right when the mass is high. When  $m$  passes the highest point  $\theta=180$  deg, the platform already has a positive velocity. As  $m$  moves past this point, friction forces together with actuation forces tend to decelerate the platform and even change its direction. As friction still increases eventually brings the platform to a stop. The actuation forces are now pointing to the left, and as a result, reverse platform motion is induced. Since the platform velocity became zero past the 180 deg point, there is less time for it to accelerate in the opposite direction and, finally, return back to its initial position before stopping again. Therefore, once a cycle is completed, the platform exhibits a net displacement as shown in Fig. 2(e). It is easy to see that if the rotational velocity of the eccentric mass increases, then platform velocity becomes zero at a point even further past the 180 deg point, increasing the net platform displacement per cycle. Reversal of the direction of  $\omega$  will lead to a reversal of the direction of motion.

### 3 3-DOF Platform

The motion principle presented in Sec. 2 is employed here in the design of a 3-DOF mobile mini robot. The design of the mini robot must meet the following design objectives: The platform should be capable of performing  $x, y, \theta$  motion. It should be able to reach positioning resolution of the order of submicrons. The platform should also be able to travel long distances, i.e., it should be able to scan a workspace whose area is five to ten times the dimensions of the platform. It should develop speeds of the order of several millimeters per second. Its size should be less than  $5 \text{ cm}^2$  so that multirobot cooperation within a workspace of limited area would be feasible. Finally, the cost of constructing and powering the platform should be as small as possible.

**3.1 Platform Base.** The geometry of the base of the micro-robot is an equilateral triangle of length  $l$ . Three small rigid supports A, B, and C located at each vertex of the triangle provide the contact points between the platform and the ground; see Fig. 3(a). The three-contact point configuration is favored due to the fact that it is not overconstrained and ensures static equilibrium along the vertical axis. For reliable open-loop response of the platform, the center of mass (CM) of the base of the platform is chosen to coincide with the geometrical center of the equilateral triangle.

**3.2 Actuators.** The actuation of the platform employs miniature-vibrating motors. The vibrating motor is axially coupled to an eccentric mass (imbalance) (see Fig. 3(b)), and the control input is the motor spin speed  $\omega$ . During rotation, the eccentric mass generates dynamic forces, which are applied to the platform.

Three identical vibrating motors D, E, and F are symmetrically mounted on top of the platform as shown in Fig. 4. If actuators D and F spin at an opposite sense of rotation while E is inactive, then the platform slides along the positive  $x$ -axis, if their sense of rotation is reversed then sliding occurs along the negative  $x$ -axis. Similarly when motors D and E or E and F spin at the same speed

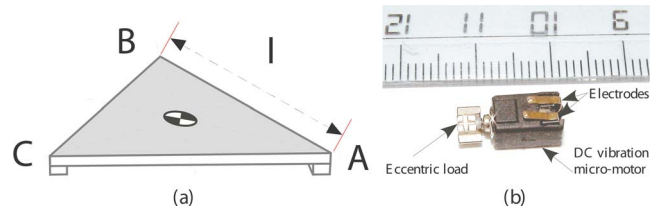


Fig. 3 (a) Platform base, (b) vibrating motor, 8 mm long

and opposite sense of rotation, pure translational motion is induced at an angle of 120 deg or 240 deg with respect to the  $x$ -axis, respectively. When D, E, and F motors spin at the same speed and at the same sense of rotation, then pure rotation about the platform CM is performed.

## 4 Dynamics

The description of the dynamics of the microrobotic platform requires the use of three dynamic models:

1. The platform dynamics, which are expressed through the corresponding equations of motion.
2. A mass-spring system that models the deformations of the platform base. The consideration of the platform as a deformable object through the mass-spring system is required in order to solve the 3 deg indeterminate problem of the static equilibrium equations and is used only during static equilibrium. Otherwise the platform is considered to be a rigid body.
3. A dynamic model describing the response of the DC vibration micromotor.

**4.1 Platform Dynamics.** The assumptions on which the platform dynamic model is based are: (i) The imbalance load can be modeled as a point mass  $m$ , rotating at a distance  $r$  from the motor axis. (ii) All actuators are identical. (iii) Every rotating mass  $m$  rotates at a constant angular speed  $\omega$  and the plane of rotation is normal to the plane of the base. (iv) All rotating masses are in phase. (v) For reasons of simplicity, it is assumed that the contact points of the platform experience Coulomb friction with a constant friction coefficient  $\mu$ . Later it will be shown that assumptions (iii) and (iv) may be relaxed.

The platform analysis involves the body-fixed frame  $B_{xy}$  and the inertial frame  $O_{xy}$ ; see Fig. 4. The adopted notation is  ${}^i f_j$ , where  $i$  is the frame index and  $j$  is the component  $x, y, z$  index. The  $b$  superscript denotes frame B. Frame O uses no superscript. The position vectors of the contact points A, B, and C are denoted

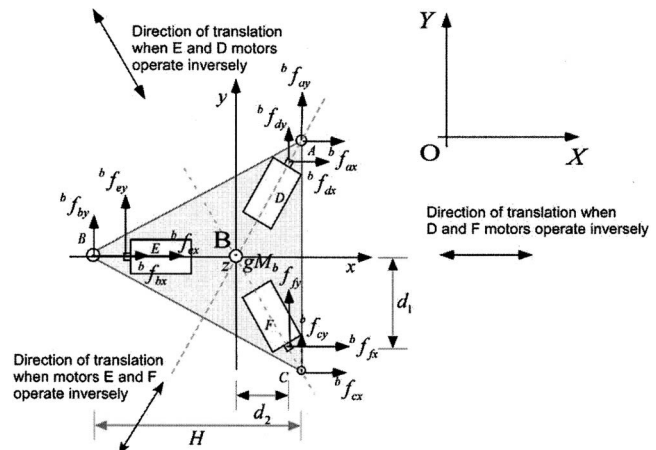
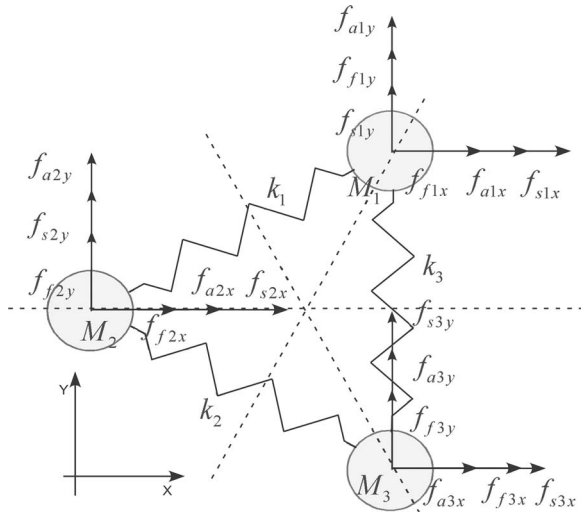


Fig. 4 Actuation and reaction forces applied to the platform



**Fig. 5 Actuation, reaction, and spring forces applied to the mass-spring model**

by  ${}^b\mathbf{r}_a, {}^b\mathbf{r}_b, {}^b\mathbf{r}_c$ , and the position vectors of the motor axis points D, E, and F on which the imbalance forces are applied are denoted by  ${}^b\mathbf{r}_d, {}^b\mathbf{r}_e, {}^b\mathbf{r}_f$ . Forces  ${}^b\mathbf{f}_a, {}^b\mathbf{f}_b, {}^b\mathbf{f}_c$  include the normal and frictional contact forces at contact points A, B, and C, respectively. The angle  $\theta$  is the eccentric mass angle with respect to the vertical axis; see Fig. 5. Because of the rotating eccentricities, forces  ${}^b\mathbf{f}_d, {}^b\mathbf{f}_e, {}^b\mathbf{f}_f$  are applied at points D, E, and F of the platform, and moments  ${}^b\mathbf{n}_d, {}^b\mathbf{n}_e, {}^b\mathbf{n}_f$  are applied along its motor axes; see Fig. 4. Their body-fixed components are given by

$$\left. \begin{aligned} {}^b f_{ix} &= -mr\omega^2 \sin \phi_i \sin \theta \\ {}^b f_{iy} &= mr\omega^2 \cos \phi_i \sin \theta \\ {}^b f_{iz} &= -mg - mr\omega^2 \cos \theta \\ {}^b n_{ix} &= -mgr \cos \phi_i \sin \theta \\ {}^b n_{iy} &= -mgr \sin \phi_i \sin \theta \\ {}^b n_{iz} &= 0 \end{aligned} \right\} i = \{d, e, f\} \quad (6)$$

where  $\omega = \dot{\theta}$  is motor angular velocity,  $r$  is the eccentricity of the imbalance mass  $m$  and  $\phi_i = \{60 \text{ deg}, 180 \text{ deg}, -60 \text{ deg}\}$  are the angles of position vectors  ${}^b\mathbf{r}_d, {}^b\mathbf{r}_e, {}^b\mathbf{r}_f$ . Then, the Newton-Euler equations of the platform are written as [18]

$$\mathbf{M}\dot{\mathbf{v}} = \mathbf{R} \sum_i {}^b\mathbf{f}_i, \quad i = \{a, b, c, d, e, f\} \quad (7a)$$

$$\begin{aligned} {}^b\mathbf{I}\dot{\boldsymbol{\omega}}_p + {}^b\boldsymbol{\omega}_p \times {}^b\mathbf{I}\boldsymbol{\omega}_p &= \sum_i ({}^b\mathbf{r}_i \times {}^b\mathbf{f}_i) + \sum_i {}^b\mathbf{n}_i \\ i &= \{a, b, c, d, e, f\}, \quad j = \{d, e, f\} \end{aligned} \quad (7b)$$

where  $\mathbf{R}$  is the rotation matrix between frames B and O,  $\boldsymbol{\omega}_p$  is the platform angular velocity,  ${}^b\mathbf{I}$  is its inertia matrix, and  $\mathbf{v} = [\dot{x}, \dot{y}, \dot{z}]^T$  is its CM position in the inertial frame. Because of platform symmetry and planar motion,  $\boldsymbol{\omega}_p = [0, 0, \dot{\psi}]$ , the term  ${}^b\boldsymbol{\omega}_p \times {}^b\mathbf{I}\boldsymbol{\omega}_p$  is zero, and Eq. (7b) reduces to a scalar equation involving the platform polar moment of inertia,  $I_{zz}$ , and moments about the z-axis

$$I_{zz}\ddot{\psi} = \hat{\mathbf{z}} \cdot \sum_i ({}^b\mathbf{r}_i \times {}^b\mathbf{f}_i), \quad i = \{a, b, c, d, e, f\} \quad (8)$$

where  $\hat{\mathbf{z}}$  denotes the unit z-axis vector.

**4.2 Deformable Body Dynamics.** When the actuation forces applied on the platform are not sufficient to overcome the static

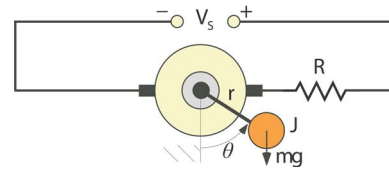


**Fig. 6 Schematic representation of the lump parameter model of the actuator**

friction forces, the platform does not slide. As the actuation forces increase, the forces distributed to the platform legs reach the Coulomb level and motion is impending. In order to conceive the way the platform shall pass from static equilibrium to motion, it is necessary to determine at which legs loss of static equilibrium will occur first. For example, if only two legs out of three begin to slide, then, inevitably, the platform shall perform a constrained motion about the third leg whose static equilibrium has not yet been lost. To this aim, it is required to have knowledge of the force distribution on each of the three supports A, B, and C of the triangular platform.

The vertical reaction forces together with the friction forces at each of the three legs constitute nine unknowns in the six static equilibrium equations. Hence, solving the static equilibrium problem results in three unknown friction forces, i.e., the rigid-body platform is statically indeterminate. These three unknowns can be determined by considering small deformations along the base of the platform. For this purpose, the platform is modeled as a lumped system, consisting of three point masses connected via stiff springs; see Fig. 5. The lumped masses  $M_1 = M_2 = M_3$ , whose aggregate equals the mass  $M$  of the base, are located at the tips of an equilateral triangle, and the springs have constants  $k_1 = k_2 = k_3$ . The produced deformations are adequately small so that the change in the angle of the springs is considered negligible. forces  $\mathbf{f}_{ai}, \mathbf{f}_{fi}, \mathbf{f}_{si}$  with  $i = \{1, 2, 3\}$ , are the actuation, friction, and spring forces exerted at mass  $i$ . The dynamic equations of the spring-mass system are

$$\begin{aligned} \mathbf{M}\ddot{\mathbf{x}} &= \mathbf{A}\mathbf{x} + \mathbf{f}_a + \mathbf{f}_f \\ \mathbf{x}(0) &= \mathbf{0} \end{aligned} \quad (9)$$

$$\dot{\mathbf{x}}(0) = \mathbf{0}$$

where  $\mathbf{M}$  is the mass matrix,  $\mathbf{A}$  is a matrix containing spring constants (see Appendix), and  $\mathbf{x} = [x_1, x_2, x_3, y_1, y_2, y_3]^T$  represents the x-y displacement of the three masses. When the masses are in a static state, the unknowns of the system are the six friction forces, which are determined by solving the six static equilibrium equations. In the case where some or all of the masses are in motion, then the magnitude of the corresponding friction forces is determined by the static friction limit (i.e., the vertical reactions times the coefficient of friction  $\mu$ ), whereas the direction of the friction forces is determined by the velocity of the corresponding mass.

**4.3 Actuator Dynamics.** The actuator is modeled as a system comprising a DC permanent magnet motor and an imbalanced load  $m$ ; see Fig. 6. The input to the actuator is the voltage  $V_s$ . The DC motor equations that relate voltage and current to speed and torque are

$$\begin{aligned} \omega &= \dot{\theta} = k_T^{-1}e \\ T &= ik_T \end{aligned} \quad (10)$$

$$e = V_s - iR$$

where  $k_T$  is the torque constant of the DC motor,  $R$  is its ohmic resistance,  $i$  is the motor current,  $e$  is the armature voltage, and  $T$

is the torque of the motor. If the viscous friction exerted on the axis of the DC motor and the inductance of the windings of the motor are considered negligible, then the dynamics of the actuator with respect to  $\theta$  are expressed through the following equation:

$$\ddot{\theta} = -\frac{k_T^2}{RJ}\dot{\theta} - \frac{mgr}{J} \sin \theta - \left(\frac{c}{J} + \frac{b}{J}\dot{\theta}\right) + \frac{k_T}{RJ}V_s \quad (11)$$

where  $J$  is the inertia of the eccentric load, and term  $((c/J) + (b/J)\dot{\theta})$  is the Coulomb and viscous friction.

## 5 Modes of Operation

In this section, the basic motion capabilities of the microrobotic platform are examined. For reasons of simplicity and for exploiting the merits of an analytical solution, only the cases of pure rotation and pure translation of the platform are examined.

If at least one of the actuators is spinning, then the platform is said to be in operation. The feasible driving speeds  $\omega$  define three modes of operation according to the type of motion (or no motion) that is induced to the platform. These are (a) the static mode, (b) the closed orbit mode, and (c) the locomotion mode.

**5.1 Static Mode of Operation.** As stated in Sec. 2, if  $\omega$  is below a critical value  $\omega_{sl}$  (i.e.,  $0 < \omega \leq \omega_{sl}$ ), then the actuation forces are not large enough to induce motion. This is the first mode of operation, called the *static mode*. In order to derive an analytical expression for  $\omega_{sl}$ , consider first the case of pure translation along the  $x$ -axis, where actuators D and F operate at the same spinning speed  $\omega = \omega_{sl}$  and at an opposite sense of rotation. Sliding is impeding, and friction forces have reached the static limit

$${}^b f_{ax} + {}^b f_{bx} + {}^b f_{cx} = \mu({}^b f_{az} + {}^b f_{bz} + {}^b f_{cz}) \quad (12)$$

Substituting Eq. (6) into Eq. (12) and solving for  $\omega$  yields

$$\omega_{sl} = \left( \frac{\mu g(M + 3m)}{mr(\sqrt{3} \sin \theta - 2\mu \cos \theta)} \right)^{1/2} \quad (13)$$

From Eq. (13), it is evident that for every  $\theta$  there is a particular critical speed  $\omega_{sl}$ . Since the rotating masses describe complete circles, it is necessary to determine the angle  $\theta$  at which the minimum  $\omega_{sl}$  occurs. Differentiating Eq. (13) with respect to angle  $\theta$  and setting the result equal to zero yields the angle of minimum  $\omega_{sl}$

$$\theta_{\omega_{sl} \min} = \tan^{-1} \left( -\frac{\sqrt{3}}{2\mu} \right) \quad (14)$$

Substituting Eq. (14) into Eq. (13) and after simple algebraic manipulations, the minimum critical speed for translation is obtained

$$\omega_{sl \min \text{ trans}} = \left( \frac{\left( \frac{2\mu}{\sqrt{3}} \right) g(3m + M)}{2mr \sqrt{1 + \left( \frac{2\mu}{\sqrt{3}} \right)^2}} \right)^{1/2} \quad (15)$$

Next, consider the case of pure rotation about the CM of the platform, where all three masses operate synchronously in a clockwise or counterclockwise direction, depending on the desired sense of rotation. Following similar reasoning with the translational case, it is found that

$$\omega_{sl \min \text{ rot}} = \left( \frac{2g(3 + M/m)}{3r(4 + a^2\mu^{-1})^{1/2}} \right)^{1/2} \quad (16)$$

**5.2 Closed Orbit Mode of Operation.** If speed  $\omega$  is greater than  $\omega_{sl}$ , then the actuation forces are large enough to counteract the friction forces and, consequently, to induce motion. It can be shown that for a small range of angular speeds  $\omega_{sl} < \omega \leq \omega_c$ , the

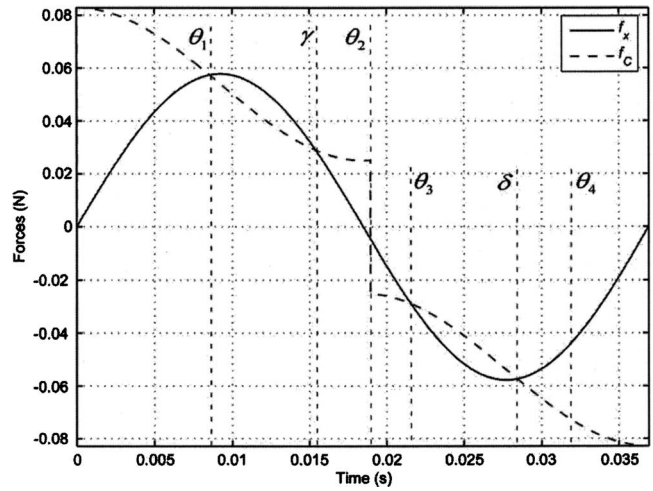


Fig. 7 Values of static friction limit and actuation forces

forward and reverse displacements per cycle are equal. Hence, the platform performs forced oscillations about a fixed point and the net displacement over time is zero. Next, the existence of this closed orbit mode of operation for  $\omega_{sl} < \omega \leq \omega_c$  is proved, analytically, and also the value of  $\omega_c$  is determined.

To this aim, Fig. 7 presents a graph of the horizontal actuation force  $f_x$ , and of the Coulomb level  $f_c$  during a full rotation of the eccentric mass (single cycle) of closed orbit mode of operation. Angle  $\theta_1$  is the point where forward sliding begins, since actuation forces overcome the Coulomb friction level. Angle  $\gamma$  is the angle at which the platform begins to decelerate, and angle  $\theta_2$  is the point where forward sliding terminates. Similarly angle  $\theta_3$  is the point where reverse sliding begins, angle  $\delta$  is the angle at which the reverse motion begins to decelerate, and  $\theta_4$  is the point where reverse motion terminates and platform comes back to rest. The angles  $\theta_1$ ,  $\gamma$ ,  $\theta_2$ ,  $\delta$ , and  $\theta_3$  depend only on the angular speed  $\omega$  of the rotating mass and platform design parameters. Figure 8 presents, schematically, one cycle of the rotating mass during closed orbit operation and relates the motion state of the platform to the angular position  $\theta$  of the rotating mass  $m$ .

Assume pure translational motion along the positive  $x$ -axis, i.e., the masses at motors D and F rotate at a constant speed  $\omega$  and with opposite sense of rotation. The resultant forces  $F_f(\theta)$  for the forward sliding and  $F_r(\theta)$  for the reverse sliding along the  $x$ -direction can be written as

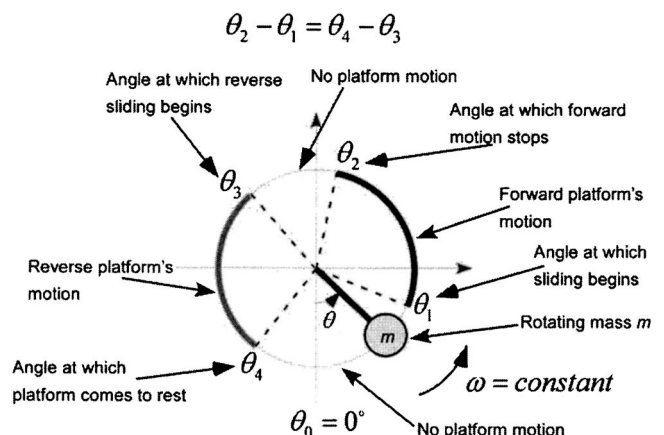


Fig. 8 A complete cycle during closed orbit operation

$$F_f(\theta) = -\mu g(3m + M) + mr\omega^2(-2\mu \cos \theta + \sqrt{3} \sin \theta) \quad (17)$$

$$F_r(\theta) = \mu g(3m + M) + mr\omega^2(2\mu \cos \theta + \sqrt{3} \sin \theta)$$

Setting Eqs. (17) to zero and solving for  $\theta$  yields

$$\theta_1 = \alpha - \cos^{-1}(\lambda/\rho), \quad \gamma = \alpha + \cos^{-1}(\lambda/\rho) \quad (18)$$

$$\theta_3 = 2\pi - \gamma, \quad \delta = -\theta_1 \quad (19)$$

where  $\alpha = \pi - \tan^{-1}[\sqrt{3}/(2\mu)]$ ,  $\lambda = \mu g(3m + M)/(mr\omega^2)$ ,  $\rho = (4\mu^2 + 3)^{1/2}$ . The corresponding expression for the velocity of forward motion is given by

$$\begin{aligned} v_f(t) &= \frac{1}{M} \int_{t_1}^t F_f dt \Rightarrow v_f(\theta_1 + \phi) = \frac{1}{M\omega} \int_{\theta_1}^{\theta_1 + \phi} F_f d\theta \\ &= \frac{1}{M\omega} \left\{ -\mu g(3m + M)\phi \right. \\ &\quad \left. + 2mr\omega^2 \sin \frac{\phi}{2} \left[ -2\mu \cos \left( \frac{\phi}{2} + \theta_1 \right) + \sqrt{3} \sin \left( \frac{\phi}{2} + \theta_1 \right) \right] \right\} \\ &= \frac{1}{M\omega} \left\{ -\mu g(3m + M)\phi \right. \\ &\quad \left. + 2mr\omega^2 \sin \frac{\phi}{2} \rho \cos \left[ \frac{\phi}{2} + (\theta_1 - \alpha) \right] \right\} \quad (20) \end{aligned}$$

where  $\phi$  is the angle past  $\theta_1$  traveled by the rotating mass  $m$ .

Substituting Eq. (18) into the right-hand side of Eq. (20) yields

$$\begin{aligned} v_f(\theta_1 + \phi) &= (M\omega)^{-1} \left[ -\mu g(3m + M)\phi \right. \\ &\quad \left. + 2mr\omega^2 \sin \frac{\phi}{2} \rho \cos \left( \frac{\phi}{2} - k \right) \right] \quad (21) \end{aligned}$$

with

$$k = \cos^{-1} \left[ \frac{\mu g(3m + M)}{mr\omega^2 \sqrt{3 + 4\mu^2}} \right]$$

Following similar reasoning, the expression for the reverse motion velocity is given by

$$v_r(\theta_3 + \psi) = (M\omega)^{-1} \left[ \mu g(3m + M)\phi - 2mr\omega^2 \sin \frac{\psi}{2} \rho \cos \left( \frac{\psi}{2} - k \right) \right] \quad (22)$$

where  $\psi$  is the angle past  $\theta_3$  traveled by the rotating mass  $m$ . From Eqs. (21) and (22), it is evident that for  $\phi = \psi = \xi$

$$v_f(\theta_1 + \xi) = -v_r(\theta_3 + \xi) \quad (23)$$

Consider

$$\begin{aligned} v_f(\theta_1 + \phi) &= 0 \\ v_r(\theta_3 + \psi) &= 0 \quad (24) \end{aligned}$$

Each of Eqs. (24) has only two solutions. The first solution is at  $\theta = \theta_1$  and  $\theta = \theta_3$ , respectively, i.e., for  $\phi = 0$  and  $\psi = 0$ . The second solution of Eq. (24) is  $\phi = \theta_2 - \theta_1$  and  $\psi = \theta_4 - \theta_3$ , respectively. Now, if  $\theta_2 - \theta_1 \neq \theta_4 - \theta_3$ , then, according to Eq. (23), each of Eqs. (24) would possess three solutions and not two, which is impossible. Therefore,  $\theta_2 - \theta_1 = \theta_4 - \theta_3$ , i.e., the angle described by the eccentric mass  $m$  during the forward motion of the platform is equal to that described during the reverse motion; see Fig. 8. Next, Eqs. (21) and (22) are integrated to give the expressions for the forward and reverse displacements

$$\begin{aligned} x_f(\theta_1 + \phi) &= (M\omega)^{-1} \left[ -g(3m + M)\phi^2 \mu \right. \\ &\quad \left. + 2mr\rho\omega^2 (\cos k - \cos(k - \phi) + \phi \sin k) \right] \quad (25) \end{aligned}$$

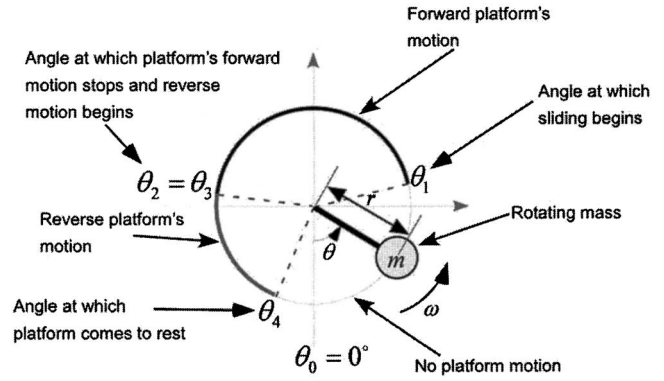


Fig. 9 A complete cycle during locomotion mode of operation

$$\begin{aligned} x_r(\theta_3 + \psi) &= (M\omega)^{-1} \left[ g(3m + M)\psi^2 \mu - 2mr\rho\omega^2 (\cos k - \cos(k - \psi) \right. \\ &\quad \left. + \psi \sin k) \right] \quad (26) \end{aligned}$$

Equation (25) and (26) show that for  $\phi = \theta_2 - \theta_1$  and  $\psi = \theta_4 - \theta_3$ ,  $x_f = -x_r$ , and therefore, the net displacement during this mode of operation is zero.

As the angular speed  $\omega$  of mass  $m$  increases, the angles  $\phi = \theta_2 - \theta_1$  and  $\psi = \theta_4 - \theta_3$  increase as well, and  $\theta_2$  approaches  $\theta_3$ . The upper limit of the closed orbit mode is the angular speed  $\omega_c$  at which  $\theta_2 = \theta_3$ . Then,

$$\phi = \theta_2 - \theta_1 \Rightarrow \phi = \theta_3 - \theta_1 \Rightarrow \phi = 2(\pi - \alpha) \Rightarrow \phi = 2 \tan^{-1}[\sqrt{3}/(2\mu)] \quad (27)$$

Substituting Eq. (27) into the first of Eqs. (24) and solving for  $\omega$  gives the maximum rotational velocity  $\omega_c$  of the closed orbit mode for pure translation

$$\begin{aligned} \omega_c &= \sqrt{\frac{\mu g(3m + M)}{2mr} \{3 - 4\sqrt{3}\mu \cot^{-1}(2\mu/\sqrt{3}) \} \\ &\quad + (3 + 4\mu^2)[\cot^{-1}(2\mu/\sqrt{3})]^2}^{1/4} \quad (28) \end{aligned}$$

Following similar arguments, it can be shown that a closed orbit mode exists also for the case of pure rotational motion.

**5.3 Locomotion Mode.** For values of  $\omega \geq \omega_c$ ,  $\theta_2 = \theta_3$  and the angle  $\theta_2 - \theta_1$  increases while the angle  $\theta_4 - \theta_3$  reduces. This means that most of the force generated by the rotating masses during one cycle is spent on accelerating and decelerating the platform during forward motion. On the contrary, relatively smaller forces accelerate and decelerate the platform in the reverse direction and for a smaller time duration. Hence, smaller speeds develop during the reverse motion. As a result, the forward displacement is greater than the reverse one and the platform exhibits a net displacement during a pure translation mode of operation, or a net change of angle during a pure rotation mode of operation.

However, if  $\omega$  is very large (i.e., if it exceeds the critical value  $\omega_{tip}$ ), then *tipping* occurs and platform stability is lost. Therefore, an upper limit for the useful motor angular velocities exist. The range of the driving speeds  $\omega \in [\omega_c, \omega_{tip}]$  is defined as the locomotion range of the platform. Figure 9 depicts a complete cycle at the locomotion mode of operation. From a design point of view, the objective is to choose platform parameter values such that the displacement per cycle is maximized. The values  $\omega_{sl}$  and  $\omega_c$  are similar functions of the parameters  $\mu, r, m, M$ ; therefore, the goal can be summarized as the maximization of the angular velocity range  $\omega \in [\omega_{sl}, \omega_{tip}]$ .

To this aim, analytical expressions are derived that relate the minimum  $\omega_{tip}$  to platform's physical parameters. Also, the analytical expression for the total displacement per cycle is derived and

its relation to the design parameters is examined.

In the case of tipping, the equilibrium of moments about the  $y$ -axis is marginally stable and reactions  $b_{f_{az}}$  and  $b_{f_{cz}}$  are reduced to zero. Taking moments about contact point B and solving for  $\omega_{\text{tip}}$  yields

$$\omega_{\text{tip}} = \left( \frac{-gHm(3+M)}{mr[2\cos\theta(H+3d_2) + 3\sqrt{3}\sin\theta h_o]} \right)^{1/2} \quad (29)$$

where parameter  $H$  is the height of the triangular base and parameter  $h_o$  is the distance between the motor axes and the ground; see Fig. 4. Differentiating Eq. (29) with respect to angle  $\theta$  and setting the result equal to zero yields the angle of minimum  $\omega_{\text{tip}}$

$$\theta_{\text{tip min}} = \tan^{-1} \left( \frac{3\sqrt{3}h_o}{2(H+3d_2)} \right) \quad (30)$$

Substituting Eq. (30) into Eq. (29) and writing  $d_2 = aH$ , where parameter  $a \in [0, 1/3]$  is a constant of proportionality, results to

$$\omega_{\text{tip min trans}} = \left( \frac{(1+3a)^{-1}2H(1+3a)g(3m+M)}{2mr\{(3\sqrt{3}h_o)^2 + [2H(1+3a)]^2\}^{1/2}} \right)^{1/2} \quad (31)$$

Using Eqs. (15) and (31), the condition for  $\omega_{s/\text{min}} < \omega_{\text{tip min}}$  yields

$$\left( \frac{\sqrt{3}}{2\mu} \right)^2 + 1 \geq \left( \frac{3\sqrt{3}h_o}{2H} \right)^2 + (1+3a)^2 \quad (32)$$

Equation (32) is a design condition, which must be met to ensure that slip occurs prior to tip during linear motion. In the case of pure rotation, where all masses rotate at the same angular velocity, platform performs hopping instead of tipping. Following similar reasoning with the translational case, it is found that for pure rotation,  $\omega_{\text{hop}}$  is given by

$$\omega_{\text{hop}} = \left( \frac{g(3+M/m)}{3r} \right)^{1/2} \quad (33)$$

Equations (16) and (33) are also taken into account to the selection of parameters  $\mu$ ,  $r$ ,  $m$ , and  $M$ .

The net displacement per cycle is found as follows. As was done previously, a single motion step of the platform is broken up into the forward phase (forward displacement) and the reverse phase (reverse displacement).

Starting from the forward phase, the slip angle  $\theta_1$  for any  $\omega \in (\omega_c, \omega_{\text{tip}})$  is derived from Eq. (13)

$$\theta_1 = f^{-1}(\omega) \quad (34)$$

Then, the linear acceleration of the forward phase is integrated with respect to  $\theta$  and yields (all motion variables are expressed with respect to frame  $O$ )

$$v_{\text{forward}}(\theta') = \frac{1}{M\omega} \int_{\theta_1}^{\theta'} (\ddot{x}_{\text{forward}}) d\theta \quad (35)$$

where  $x_{\text{forward}}$  is the displacement along the direction of motion. Next,  $v_{\text{forward}}(\theta') = 0$  is solved for  $\theta'$ . Setting next  $\theta_2 = \theta'$ , and integrating  $v$  from  $\theta_1$  to  $\theta_2$  yields

$$x_{\text{forward}} = \frac{1}{M\omega^2} \int_{\theta_1}^{\theta_2} v_{\text{forward}}(\theta') d\theta' \quad (36)$$

At an angle  $\theta_2$ , where  $\theta_2 = \theta_3$  (see Fig. 9), the forward phase ends and the reverse phase begins. Repeating the previous steps for the reverse phase yields

$$x_{\text{reverse}} = \frac{1}{M\omega^2} \int_{\theta_2}^{\theta_4} v_x(\theta') d\theta' \quad (37)$$

Hence, the net displacement is a function of  $\omega$  and is given by

$$x_{\text{total}} = x_{\text{forward}} + x_{\text{reverse}} \Rightarrow x_{\text{total}}$$

$$\begin{aligned} &= \frac{1}{2M\omega^2} (-\mu g(3m+M)(\theta_1 - \theta_4)(\theta_1 - 2\theta_2 + \theta_4) \\ &\quad + 2mr\omega^2 \{-2\mu[\cos\theta_1 - 2\cos\theta_2 + \cos\theta_4 + (\theta_1 - \theta_2)\sin\theta_1 \\ &\quad - (\theta_2 - \theta_4)\sin\theta_2] + \sqrt{3}[(-\theta_1 + \theta_2)\cos\theta_1 \\ &\quad - (\theta_2 - \theta_4)\cos\theta_2 + \sin\theta_1 - \sin\theta_4]\}) \end{aligned} \quad (38)$$

Similarly, the net rotational motion is given by

$$\begin{aligned} \psi_{\text{total}} &= \frac{1}{3I\omega^2} (\mu H \{-g(3m+M)(\theta_1 - \theta_4)(\theta_1 - 2\theta_2 + \theta_4) \\ &\quad - 6mr\omega^2[\cos\theta_1 - 2\cos\theta_2 + \cos\theta_4 + (\theta_1 - \theta_2)\sin\theta_1 \\ &\quad - (\theta_2 - \theta_4)\sin\theta_2]\} - 3mr\omega^2[(\theta_1 - \theta_2)\cos\theta_1 \\ &\quad + (\theta_2 - \theta_4)\cos\theta_2 - \sin\theta_1 + \sin\theta_4](\sqrt{3}d_1 + 3d_2)) \end{aligned} \quad (39)$$

where the values  $d_1$ ,  $d_2$ , and  $H$  are defined in Fig. 4.

It should be emphasized that the motion mechanism is strictly based on sliding. Hopping or tipping are undesirable effects, and therefore, they should not be allowed to occur. This is achieved by keeping the micromotor angular speed  $\omega$  below the threshold limits derived for the translational and rotational cases, see Eqs. (31) and (33), respectively. Since the platform does not exhibit hopping or tipping, it is not necessary to use equations of motion that describe rigid-body three-dimensional (3D) motion.

## 6 Design Parameters

The equations derived above provide a number of design guidelines. Indeed, from Eqs. (32) and (33) it is clear that in order to increase  $\omega_{\text{tip}}$  (or  $\omega_{\text{hop}}$ ), parameter  $H$  or, equivalently, the base surface should be maximized and parameter  $h_o$  (i.e., the motor height) should be minimized. The material at the contact points should exhibit a low coefficient of friction in order to increase the total displacement per step, as indicated by Eqs. (38) and (39). The parameter  $r$ , according to Eqs. (38) and (39), is proportional to the total displacement per cycle, but according to Eqs. (31) and (33),  $\omega_{\text{tip}}$  is inversely proportional to  $\sqrt{r}$ . An average value of  $r$  is selected in order to increase the step length per cycle without substantially reducing the value of  $\omega_{\text{tip}}$ .

The above design rules apply to both the translational and rotational motion, and it is evident that they extend to the general plane motion. On the otherhand, increasing the value of parameter  $a$  decreases  $\omega_{\text{tip trans}}$  but increases the value of  $\omega_{\text{tip rot}}$ . Hence, an average value of parameter  $a$  is desired in order to keep balance between the translational and rotational operating ranges. It should be mentioned that to keep the working area for microbotics applications limited, the platform side length should not exceed 5 cm and, consequently, this imposes an upper limit to parameter  $H$ . Finally, from Eqs. (38) and (39), it is observed that mass  $M$  and inertia  $I$  should be kept low; otherwise the net displacement is reduced considerably. Specifically, the platform mass  $M$  should not exceed 0.2 kg and inertia  $I_{zz}$  should be  $< 10^{-4}$  kg m<sup>2</sup>.

The choice of the vibrating micromotor should render feasible the generation of the required actuation forces in order to drive the platform into the locomotion mode of operation. Equation (11) and the analytical expressions of the related critical speeds  $\omega_c$ ,  $\omega_{\text{tip}}$  result into appropriate selection of micromotor nominal speed and eccentric load. Also, the electrical characteristics of the micromotor should allow for a low-voltage single-cell untethered power supply. A typical vibrating micromotor that complies with the above guidelines and the dimensional constraints of the platform is the 4TH9-3006A coreless vibration motor of Jinlong Machinery & Electronics Co. whose mechanical and electrical characteristics are given in Table 1.

**Table 1 Vibrating motor SE-S4E specifications**

Parameter	Value	Parameter	Value
Operating voltage (V)	~1.4	Weight of motor (g)	0.95
Starting voltage (V)	0.8	Motor diameter (mm)	4
Starting current (mA)	110	Motor length (m)	14.4
Armature resistance ( $\Omega$ )	10	Nominal speed (rpm)	10,000

The particular vibration micromotor is designed to produce small vibrations to mobile phones of mass 0.08 kg. The consideration of the above analysis leads to the set of design parameter values listed in Table 2.

**7 Simulation**

A dynamic simulation of the generalized plane motion of the platform is implemented using MATLAB and SIMULINK. The aim of the simulation is to verify analytical results and to demonstrate the platform motion capabilities.

**7.1 Simulator Software Design.** Simulation software comprises (i) a dynamic model of the platform, (ii) a dynamic model of the deformable object, (iii) a dynamic model of the actuators and (iv) a differential kinematics model. The generalized plane motion of the platform is completely described by five motion states, depending on the speeds  $v_a$ ,  $v_b$ , and  $v_c$  at each of the support points A, B, and C, respectively; see Fig. 10. In state 0, no motion is induced to the platform. On the contrary, state 1 represents the unconstrained motion of the platform. States 2–4 represent the constraint motion about one of the platform’s supports (either A, B, or C). At every time step, the procedure presented in Fig. 11 is executed. The input to the system is either the motors’ speed or input voltage.

**7.2 Motion Examples.** The first example demonstrates the closed orbit mode of operation for pure translational motion. To this aim, it is assumed that the platform parameters are those presented in Table 2 and that motors D and F rotate at the same speed and with opposite sense of rotation. According to Eq. (28), the upper bound of the closed orbit mode is  $\omega_c=9685.6$  rpm, whereas, according to Eq. (15), the lower bound is  $\omega_{sl}=8519.4$  rpm. The motors speeds are set to  $\omega_d=-9400$  rpm and  $\omega_f=9400$  rpm. Figure 12(a) depicts the accelerations of the platform. The spikes that are observed in the acceleration graph are due to switching from the deformable object model to the rigid-body model. Figure 12(b) presents the velocity of the platform, and Fig. 12(c) its displacement. Clearly, the platform operates in

**Table 2 Design parameters**

Parameter	Value	Parameter	Value
$r$ (m)	0.00177	$l$ (m)	0.05
$m$ (kg)	0.00021	$h_o$ (m)	0.004
$M$ (kg)	0.12	$\mu$ (-)	0.5

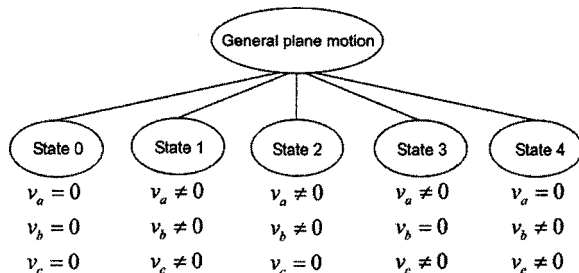


**Fig. 10 The five motion states of the platform**

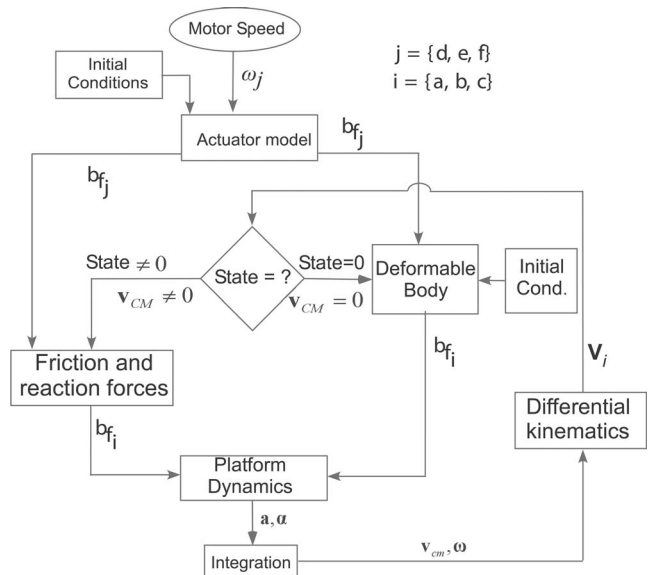


**Fig. 11 Program flowchart**

the closed orbit mode and exhibits zero net displacement. Figure 12 also depicts the six characteristic angles of a complete cycle of operation, as these were described in Sec. 5. It is interesting to observe that the graph of position exhibits, at each peak of the wave form, an upper flat region between angles  $\theta_2$  and  $\theta_3$  and a low flat region between angles  $\theta_4$  and  $\theta_1$ . As described in Sec. 5, these flat regions correspond to zero platform velocity.

Figure 13 presents the friction forces developed during the first cycle of operation. Initially, the platform is static, simulation uses the deformable object model, and friction is exerted only on legs A and C. Gradually, the actuation forces and the friction forces on legs A and C increase. At some point friction forces reach the Coulomb level, then the platform starts to deform and forces are transmitted to leg C. When friction at all three legs has reached the Coulomb level, the platform accelerates, forward motion along the  $x$ -axis is induced, and simulation switches to the rigid-body model. In a similar manner, the program alternates between deformable and rigid-body models during the rest of the simulation.

The second simulation example demonstrates pure translation at a direction 120 deg with respect to the  $x$ -axis. To this aim, rotational speeds of motors D and E are set at constant speeds of  $\omega_d=10,218$  rpm and  $\omega_e=-10,218$  rpm, respectively. Figure 14(a) depicts the accelerations  $a_x$  and  $a_y$  of CM. Figure 14(b) presents the velocities  $v_x$  and  $v_y$  of CM, and Fig. 14(c) presents positions  $x$  and  $y$  of CM. From Fig. 14(c), it is evident that the platform exhibits a net displacement, and hence, it operates in the locomotion mode. It can be observed that the displacement wave form does not exhibit flat peaks. This stems from the fact that  $\theta_2=\theta_3$  (see Fig. 9), i.e., the platform goes directly from the forward motion to the reverse motion without stopping in between. Finally, in Fig. 14(d), the path of the platform in the  $x$ - $y$  plane is presented.

In the third example, the platform performs a pure rotation. All motors spin at  $\omega=9740$  rpm. Figure 15(a) depicts the angular displacement  $\psi$  of the platform, whereas Fig. 15(b) presents the platform angular velocity.

The fourth example again demonstrates pure translation along the  $x$ -axis, but this time the rotating masses of motors D and F exhibit a small phase difference of 5 deg; see Fig. 16. Because of this difference, the resultant moments about the CM of the platform and the resultant forces along the  $y$  direction are not zero. Consequently, motion along the  $y$ -axis and rotation about platform’s CM is induced; see Figs. 16(b) and 16(c). However, it is observed that these parasitic motions have small magnitude, and most importantly, the motion along the  $x$ -axis is almost preserved;

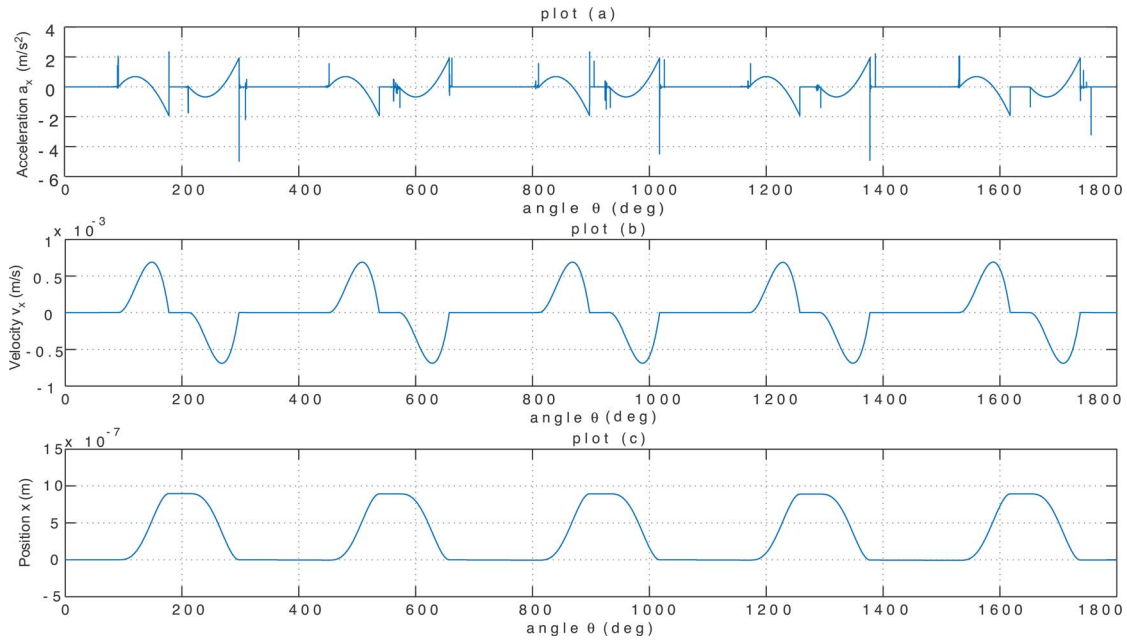


Fig. 12 Closed orbit simulation

see Fig. 16(a). If the phase difference of the spinning masses increases, the efficiency of the motion mechanism is reduced, i.e., the desired displacement is reduced while the parasitic motions grow bigger. The worst case appears when the masses operate at 180 deg out of phase, where the actuation forces cancel each other and no translational motion is induced. In this case, the platform exhibits rotational motion. Simple electromechanical means shall be used so that the actuators start rotating in phase. This mechanism stalls the actuators at the same angle, thus eliminating the

phase difference.

The synchronization assumption, i.e., same spin speed, does not have to be strictly satisfied. Nonsynchronized actuators generate resultant actuator forces with sinusoidal beat wave forms that give rise to motions other than those desired. Similarly to the out-of-phase situation, if the asynchronies are limited, they will almost preserve the desired motion and induce limited parasitic motion. However, if the actuator open-loop rotational speeds differ considerably, then the platform's velocity error will be prohibitively

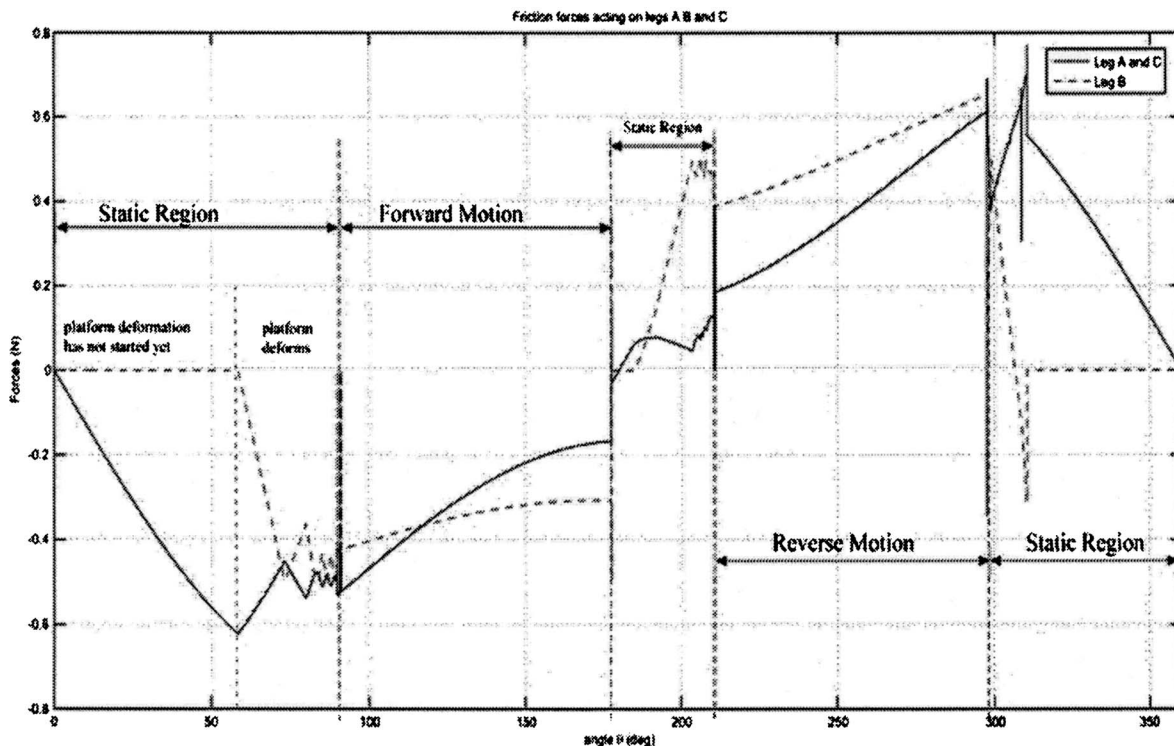


Fig. 13 Friction forces applied on legs A, B, and C

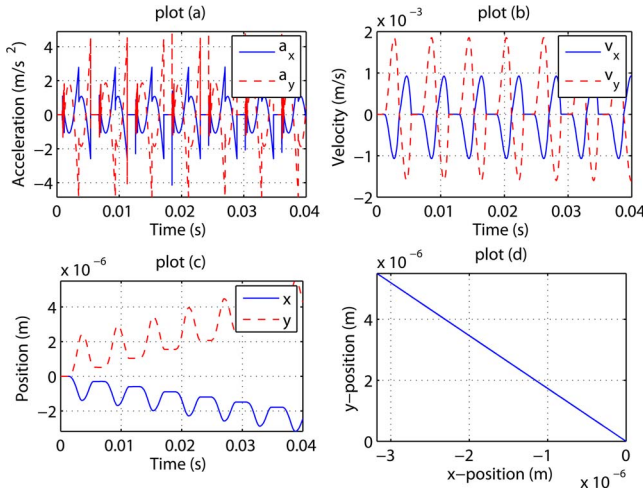


Fig. 14 Pure translation at an angle of 120 deg with respect to the x-axis

large. It is expected that the platform's actuation will suffer from some asynchronous operation, leading to a less predictable behavior. Hence, a closed-loop control strategy is required to obtain desired motion patterns. The loop can be closed either at the actuators rotational speed or at platform position. A less attractive, open-loop, alternative solution is the use of stepper, instead of DC, motor [19]. Overall, the closed-loop solution is preferable because, in addition to eliminating asynchronous operation, it can compensate for external disturbances. Another drawback of using stepper motors is their large dimensions compared to those of micro DC motors.

This final example examines the case where the rotating mass is accelerated and analyzes the transient effects that the platform exhibits. Taking into account rotating mass accelerations, and neglecting the torque due to the rotating mass, Eqs. (6) become

$$\begin{aligned} {}^b f_{ix} &= -(-mr\alpha \cos \theta + mr\omega^2 \sin \theta) \sin \phi_i \\ {}^b f_{iy} &= (-mr\alpha \cos \theta + mr\omega^2 \sin \theta) \cos \phi_i \\ {}^b f_{iz} &= -mg - mr\alpha \sin \theta - mr\omega^2 \cos \theta \end{aligned} \quad (40)$$

$$i = \{d, e, f\}, \quad \phi_i = \{60 \text{ deg}, 180 \text{ deg}, -60 \text{ deg}\}$$

where  $\alpha = \dot{\omega} = \ddot{\theta}$ . The acceleration  $\ddot{\theta}$  is generated by the micromo-

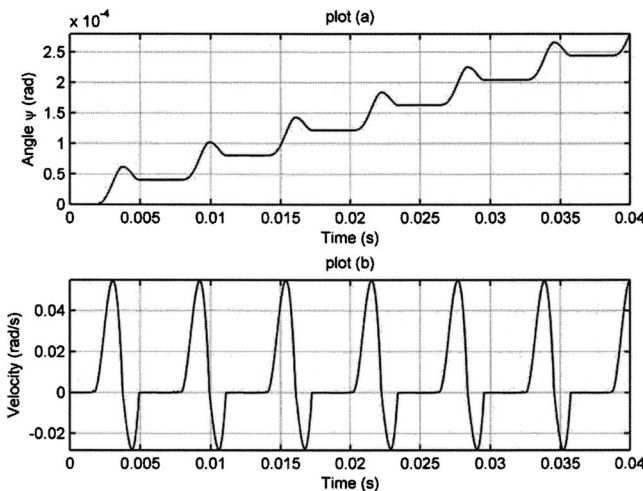


Fig. 15 Pure rotation about the z-axis

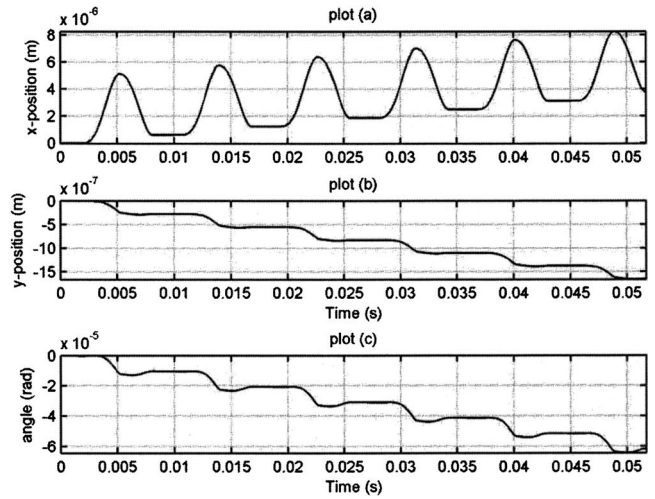


Fig. 16 Displacement when motors rotate at a phase difference of 5 deg

tor that is governed by Eq. (11).

Most of the parameters of Eq. (11) are provided by Table 2. The torque constant may be calculated by the nominal values of Table 1, according to Eqs. (10). The Coulomb level  $C$  of the micromotor can be calculated by the starting voltage given in Table 1. Finally, the viscous friction coefficient  $b$  is calculated by considering the steady state of Eq. (11). The simulation scenario is as follows: The rotating mass  $m$  accelerates for a duration of 0.52 s, from 0 rpm to 10,000 rpm, during this period, the platform passes from static mode to closed orbit mode and then to locomotion mode. At  $t=0.52$  s, the acceleration of the rotating mass  $m$  reduces to 0 for a period of  $t=0.6$  s. During this period, the platform is in steady-state operation in the locomotion mode. Finally, at  $t=1.12$  s, the rotating mass  $m$  decelerates for another 0.52 s until the rotational speed becomes 0 again. During the deceleration period, the platform gradually sweeps from locomotion mode to static mode. Figure 17(a) depicts the entire response of the platform displacement. Figure 17(b) and 17(c) depict the transient response of the platform, during acceleration and deceleration of the rotating mass  $m$ . From Fig. 17(b), one can identify the existence of all three modes of operation. First, from 0 s until 0.45 s, the platform is in static mode. From 0.45 s to  $\sim 0.52$  s, the platform exhibits a transient response. Within this transient interval, first the closed orbit

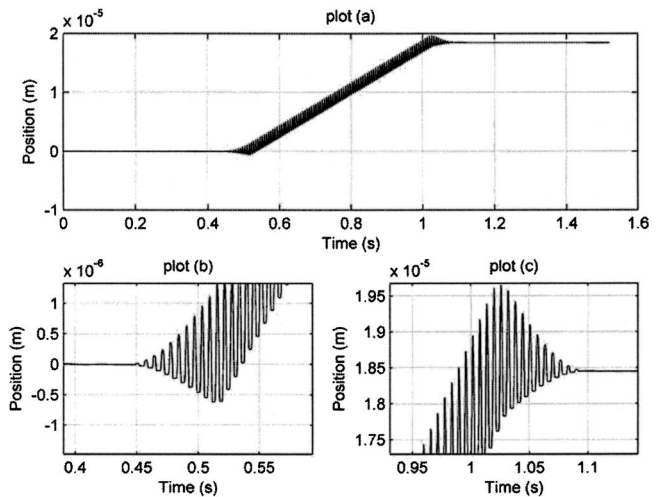


Fig. 17 Transient response of the platform during translational motion

modes and then the locomotion mode can be identified by determining whether the upper peaks of the displacement wave form are flat or not. Similar observations can be made for the deceleration region; see Fig. 17(c). By comparing the two transient regions, it can be argued that the reverse displacement that takes place during acceleration transients is compensated by the forward displacement that occurs during deceleration transients. Hence, the undesired displacement during the transient motion can be considered negligible. Of course, this assumption holds only in the case where the magnitude and duration of acceleration is equal to that of deceleration. Furthermore, it can be seen that even at an open-loop response, the transient duration that affects the motion state of the platform is limited to a few steps. This is an indication that the platform's motion resolution is slightly reduced by the transient effects.

## 8 Open-Loop Control

It is important to derive an open-loop control of the platform in order to be in position to specify the required  $\omega$  (control input) that results to the desired displacement per cycle (input command). To this aim, the inverse function  $\omega = f^{-1}(x_{\text{total}})$  is calculated numerically, where  $\omega$  is the motor angular speed and  $x_{\text{total}}$  is the net displacement produced during a cycle. Only the locomotion mode of operation is of interest. The determination of the inverse function requires the solution of a nonlinear system of four equations, which is formed by Eq. (13),  $v_{\text{forward}}(\theta_2) = 0$ ,  $v_{\text{reverse}}(\theta_4) = 0$ , and Eq. (38) expressed in the following functional form

$$\begin{aligned} f_1(\theta_1, \omega) &= 0 \\ f_2(\theta_1, \theta_2, \omega) &= 0 \\ f_3(\theta_2, \theta_4, \omega) &= 0 \\ f_4(\theta_1, \theta_2, \theta_4, \omega) &= 0 \end{aligned} \quad (41)$$

Given the desired  $x_{\text{total}}$ , the system is numerically solved for  $\omega$ . Following the same reasoning, a set of similar equations is generated for the rotational motion.

The numerical solution procedure uses an improved Newton-Raphson algorithm and requires good initial guesses of the four unknown variables:  $\theta_1, \theta_2, \theta_4, \omega$ . The initial guess for the three angles is provided by the physics of the motion mechanism, which determines the region of each angle (this applies to the entire locomotion range). For the initial guess of the rotating mass angular speed  $\omega$ , a sparse look-up table suffices. Hence, the numerical solution procedure can be automated so that open-loop control requires only a sequence of input commands.

As an example of the open-loop control efficacy, consider the case where it is desired to perform a path that comprises three parts: (i) 1000  $\mu\text{m}$  along the positive  $x$ -axis implemented through 200 steps of 5  $\mu\text{m}$ , (ii) 20 mrad clockwise about the  $z$ -axis implemented through 100 steps of 0.2 mrad, and, finally, (iii) the platform performs a translation of 10  $\mu\text{m}$  at an angle of 20 mrad with respect to the  $x$ -axis, implemented through 20 steps of 0.5  $\mu\text{m}$ . The step length values are such that they can be achieved by a range of speeds  $\omega$  close to the nominal speed; see Table 1.

Figure 18(a) presents the trajectory of the platform along the  $x$ -axis. Figure 18(b) depicts the trajectory along the  $x$ -axis only for part (iii) of the motion. Figure 18(c) amplifies a small region of Fig. 18(b) and demonstrates the high motion resolution of the platform, showing that the step size is 0.5  $\mu\text{m}$ . Hence, from Fig. 18, it can be seen that the platform is able to travel distances of the order of millimeters in a reasonable amount of time, but is also capable of performing motion of high resolution. Figure 19(a) shows the angular displacement of the platform. As expected the angular displacement occurs only during part (ii) of the path. Figure 19(b) amplifies a small region of Fig. 19(a) and demonstrates the resolution of the angular motion, showing that it is 0.2 mrad.

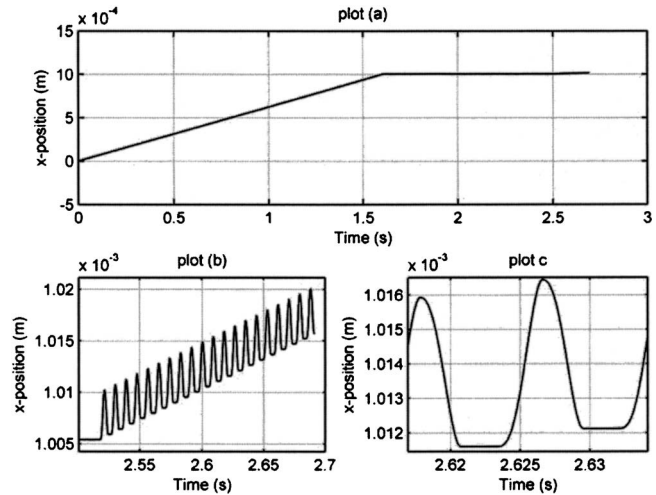


Fig. 18 Plots of the displacement along the  $x$ -axis

Inertia of the spinning mass was neglected in this example. In a hardware experiment, however, inertia will be present and the platform will exhibit transient regions during acceleration or deceleration. As it was presented in Sec. 7, even for the case of open-loop control commands, the accelerations of the micromotor are large enough so that transients do not last for more than four to five steps, and they have small effect on the platform resolution. Even more, in a closed-loop operation, the micromotor's time constant  $\tau$  will be reduced to about one cycle, leading to a practically negligible small duration of the transients.

## 9 Future Work

Future work includes the construction of the microrobotic platform, the experimental evaluation of its capabilities, and the development of closed-loop control algorithms that will compensate for parasitic motions induced due to phase differences, nonsymmetric inertial distribution, and friction nonuniformities. Furthermore, extensive analysis will be performed on the platform's behavior under asynchronous motor operation. The authors intend to study the navigation of the platform in the  $x$ - $y$  plane by exploiting such asynchronous operation under closed-loop position control. Also, of great importance is the development of a high-accuracy position feedback system. To this aim, the authors are currently working on the construction and setup of an interferometric sensor for measuring the displacement of the microrobotic platform.

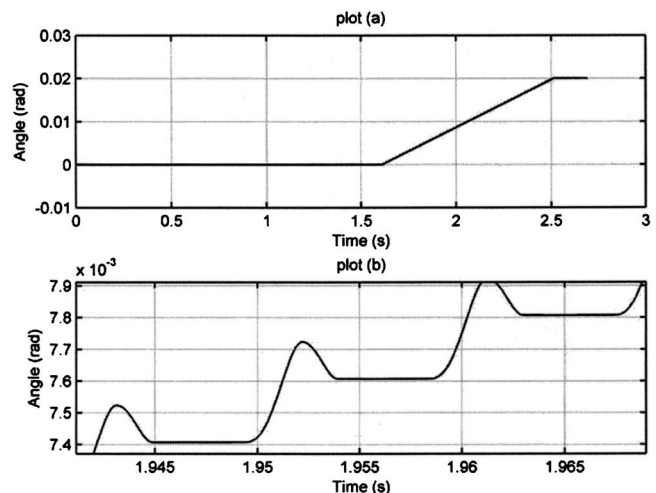


Fig. 19 Plot of the angle of the platform

## 10 Conclusions

The paper presented the dynamic analysis, design, and simulation of a novel microrobotic platform that is able to perform  $x$ ,  $y$ , and  $\theta$  motion, composed by a sequence of pure translational and rotational paths. Theoretical results suggested that the platform is capable for submicrometer position accuracy and for developing speeds up to  $\sim 1.5$  mm/s. The assertions of submicrometer positioning accuracy of the platform were based entirely on theoretical results. Nevertheless, experimental validation is certainly necessary and will be performed to provide full proof of concept. The novel motion mechanism was described and explained in detail. A nontrivial dynamic model, which comprises the rigid and deformable body of the platform, was derived. The operation modes of the platform were defined, and, accordingly, design guidelines were derived. Several design parameters, such as dimensions and weight, were specified, and a DC vibration motor adequate for inducing the desired motion to the platform was selected. All platform elements are of low cost and readily available. The power requirements of the DC vibration micromotors demand a single-cell battery of 1.5 V. The platform's motion capabilities were demonstrated and evaluated by a set of simulations. The obtained results indicate that for efficient open-loop operation of the plat-

form, the phase difference among the rotated eccentric masses should be small. This may be achieved using mechanical contacts that stall the actuators at the same angle, thus, eliminating the phase difference. Similarly, for efficient open-loop operation, actuators should operate synchronously. In practice, the actuators will exhibit asynchronous operation that will affect the platform motion. Hence, the desired motion response necessitates for closed-loop control of the platform's position. Furthermore, simulations demonstrated that, in general, the transient effects due to acceleration of the rotating masses result to a reduction of platform's motion resolution to about five steps. However, this resolution deterioration might be practically eliminated using a closed-loop operation of the DC vibration micromotors.

## Acknowledgment

The project is cofunded by the European Social Fund (75%) and National Resources (25%)-(EPEAEK II)-HRAKLEITOS.

## Appendix

The mass matrix  $M$  in Eq. (9) is given by

$$M = \text{diag}(M_1, M_2, M_3, M_4, M_5, M_6) \quad (\text{A1})$$

while the stiffness matrix in Eq. (9) is given by

$$A = \begin{pmatrix} \frac{-k_1\sqrt{3}}{2} & \frac{k_1\sqrt{3}}{2} & 0 & 0 & 0 & 0 \\ \frac{k_1\sqrt{3}}{2} & -\frac{k_1\sqrt{3}}{2} - \frac{k_2\sqrt{3}}{2} & \frac{k_2\sqrt{3}}{2} & 0 & 0 & 0 \\ 0 & \frac{k_2\sqrt{3}}{2} & -\frac{k_2\sqrt{3}}{2} & 0 & 0 & 0 \\ 0 & 0 & 0 & -k_3 - \frac{k_1}{2} & \frac{k_1}{2} & k_3 \\ 0 & 0 & 0 & \frac{k_1}{2} & -\frac{k_1}{2} - \frac{k_2}{2} & \frac{k_2}{2} \\ 0 & 0 & 0 & k_3 & \frac{k_2}{2} & -k_3 - \frac{k_2}{2} \end{pmatrix} \quad (\text{A2})$$

## References

- [1] Breguet, J.-M., and Clavel, R., 1998, "Stick and Slip Actuators: Design, Control, Performances and Applications," *Proc. International Symposium on Microelectronics and Human Science (MHS)*, Nagoya, IEEE, N.Y., pp. 89–95.
- [2] Schmoedel, F., and Fatikow, S., 2000, "Smart Flexible Microrobots for Scanning Electron Microscope (SEM) Applications," *J. Intell. Mater. Syst. Struct.*, **11**(3), pp. 191–198.
- [3] Schmoedel, F., and Worn, H., 2001, "Remotely Controllable Mobile Micro-Robots Acting as Nano Positioners and Intelligent Tweezers in Scanning Electron Microscopes (SEMs)," *Proc. International Conference on Robotics and Automation*, Seoul, IEEE, N.Y., May 21–26, pp. 3903–3913.
- [4] Büchi, R., Zesch, W., and Codourey, A., 1995, "Inertial Drives for Micro- and Nanorobots: Analytical Study," *Proc. SPIE*, **2593**, pp. 89–97.
- [5] Codourey, A., Zesch, W., Büchi, R., and Siegwart, R., 1995, "A Robot System for Automated Handling in Micro-World," *Proc. International Conference on Intelligent Robots and Systems*, Pittsburgh, IEEE, N.Y., Aug. pp. 3185–3191.
- [6] Martel, S., Sherwood, M., Helm, C., Garcia de Quevedo, W., Fofonoff, T., Dyer, R., Bevilacqua, J., Kaufman, J., Roushdy, O., and Hunter, I., 2001, "Three-Legged Wireless Miniature Robots for Mass-scale Operations at the Sub-atomic Scale," *Proc. 2001 IEEE International Conference on Robotics & Automation*, Seoul, May 21–26, IEEE, New York, pp. 3423–3428.
- [7] Simu, U., 2002, "Piezoactuators for Miniature Robots," Doctoral thesis, Department of Materials Science, Uppsala University.
- [8] Simu, U., and Johansson, S., 2002, "Fabrication of Monolithic Piezoelectric Drive Units for Miniature Robot," *J. Micromech. Microeng.*, **12**, pp. 582–589.
- [9] Simu, U., and Johansson, S., 2002, "Evaluation of a Monolithic Piezoelectric Drive Unit for a Miniature Robot," *Sens. Actuators, A*, **30**, pp. 175–184.
- [10] Aoyama, H., and Fuchiawaki, O., 2001, "Flexible Micro-Processing by Multiple Micro Robots in SEM," *Proc. 2001 IEEE International Conference on Robotics & Automation*, Seoul, Korea, May 21–26, pp. 3429–3434.
- [11] Lee, Y., Kim, B., Lee, M., and Park, J.-O., 2004, "Locomotive Mechanism Design and Fabrication of Biomimetic Micro Robot Using Shape Memory Alloy," *Proc. 2004 IEEE International Conference on Robotics & Automation*, New Orleans, April, IEEE, New York, pp. 5007–5012.
- [12] Technology Review, 2004, "Nanomanipulator," *MIT Technol. Rev.*, Oct. pp. 80–84.
- [13] Fumiya, I., Raja, D., and Chandana, R., 2002, "Design and Control of a Pendulum Driven Hopping Robot," *Proc. 2002 IEEE/RSJ International Conference on Intelligent Robots and Systems (IROS '02)*, Vol. 3, IEEE, New York, pp. 2141–2146.
- [14] Caprari, G., Arras, K. O., and Siegwart, R., 2000, "The Autonomous Miniature Robot Alice: From Prototypes to Applications," *Proc. 2000 IEEE/RSJ International Conference on Intelligent Robots and Systems (IROS '00)*, IEEE, New York, pp. 793–798.
- [15] Papadopoulos, E., and Papadimitriou, I., 2001, "Modelling, Design and Control of a Portable Washing Machine During the Spinning Cycle," *Proc. IEEE/ASME International Conference on Advanced Intelligent Mechatronics System (AIM 2001)*, Como, Italy, IEEE, N.Y., pp. 899–904.
- [16] Badami, V. V., and Chibat, N. W., 1998, "Home Appliances Get Smart," *IEEE Spectrum*, **35**(8), pp. 36–43.
- [17] Papadopoulos, E., and Chasparis, G., 2004, "Analysis and Model-Based Control of Servomechanisms With Friction," *ASME J. Dyn. Syst., Meas., Control*, **126**(4), pp. 911–915.
- [18] Sciacivco, L., and Siciliano, B., 2001, *Modelling and Control of Robot Manipulators*, Springer-Verlag, Berlin.
- [19] Wildi, T., 2002, *Electrical Machines, Drives, and Power Systems*, 5th ed., Prentice-Hall, Englewood Cliffs, NJ.